RESEARCH

High order semi-implicit weighted compact nonlinear scheme for the all-Mach isentropic Euler system

Yanqun Jiang[1*†], Xun Chen[1], Xu Zhang[1], Tao Xiong[2] and Shuguang Zhou[3]

*Correspondence: jyq2005@mail.ustc.edu.cn
[1]Department of Mathematics, Southwest University of Science and Technology, 621010 Mianyang, China
Full list of author information is available at the end of the article
†Equal contributor

Abstract

The computation of compressible flows at all Mach numbers is a very challenging problem. An efficient numerical method for solving this problem needs to have shock-capturing capability in the high Mach number regime, while it can deal with stiffness and accuracy in the low Mach number regime. This paper designs a high order semi-implicit weighted compact nonlinear scheme (WCNS) for the all-Mach isentropic Euler system of compressible gas dynamics. To avoid severe Courant-Friedrichs-Levy (CFL) restrictions for low Mach flows, the nonlinear fluxes in the Euler equations are split into stiff and non-stiff components. A third-order implicit-explicit (IMEX) method is used for the time discretization and a fifth-order WCNS is used for the spatial discretization. The designed semi-implicit WCNS is asymptotic preserving and asymptotically accurate in the zero Mach number limit. One- and two-dimensional numerical examples in both compressible and incompressible regimes are given to demonstrate the advantages of the designed method.

Keywords: High order scheme; IMEX time discretization; WCNS; Asymptotic-preserving property; Low Mach number; Isentropic Euler equations

Introduction

Low-Mach number flows in fluid dynamics that are slow compared with the speed of sound can be described by the following scaled isentropic Euler equations.

$$\begin{cases} \rho_t + \nabla \cdot (\rho \mathbf{u}) &= 0, \\ (\rho \mathbf{u})_t + \nabla \cdot (\rho \mathbf{u} \otimes \mathbf{u}) + \frac{1}{\varepsilon^2} \nabla p &= 0, \end{cases} \tag{1}$$

where $\rho(\mathbf{x}, t) > 0$, $\mathbf{u}(\mathbf{x}, t)$ and $\mathbf{q} = \rho \mathbf{u}(\mathbf{x}, t)$ are the density, velocity and momentum of the fluid, respectively, and $\varepsilon > 0$ is the scaled Mach number that is a measure of compressibility of the fluid. For example, $\varepsilon = 1$ corresponds to the fully compressible regime. The operators ∇, $\nabla\cdot$ and $\otimes$ are respectively the gradient, divergence and tensor product operators. The pressure p in Eqs. (1) is given by the equation of state

$$p(\rho) = \Lambda \rho^{\gamma}, \tag{2}$$

Research Square

Preprints are preliminary reports that have not undergone peer review. They should not be considered conclusive, used to inform clinical practice, or referenced by the media as validated information.

where $\Lambda > 0$ and $\gamma \geq 1$ are constants. Eqs. (1) are hyperbolic with wave speeds in direction $\mathbf{n}$

$$\lambda_{1,3} = \mathbf{u} \cdot \mathbf{n} \pm c, \lambda_2 = \mathbf{u} \cdot \mathbf{n}, \tag{3}$$

with the sound speed $c = \sqrt{p'(\rho)}/\varepsilon$.

Klainerman and Majda [1, 2] proved that the solutions of Eqs. (1) converge to the incompressible counterpart when $\varepsilon \sim 0$. The asymptotic nature of solutions to Eqs. (1) can be studied by plugging-in the ansatz

$$f(\mathbf{x}, t) = f_0(\mathbf{x}, t) + \varepsilon^2 f_2(\mathbf{x}, t) + O(\varepsilon^3), \tag{4}$$

for variables ρ, p and $\mathbf{u}$. After performing a scale analysis, we obtain an incompressible Euler system for the velocity

$$\begin{cases} (\mathbf{u}_0)_t + \nabla \cdot (\mathbf{u}_0 \otimes \mathbf{u}_0) + \frac{\nabla p_2}{\rho_0} &= 0, \\ \nabla \cdot \mathbf{u}_0 &= 0, \end{cases} \tag{5}$$

based on well-prepared initial data, i.e.,

$$\rho(\mathbf{x}, 0) = const + O(\varepsilon^2), \nabla \cdot \mathbf{u}(\mathbf{x}, 0) = O(\varepsilon), \tag{6}$$

and appropriate boundary conditions[3, 4], e.g., periodic, wall or homogeneous Neumann boundary conditions. Taking the divergence of the first equation in (5) and using the incompressibility, we obtain

$$\triangle p_2 = -\nabla \cdot (\nabla \cdot (\rho_0 \mathbf{u}_0 \otimes \mathbf{u}_0)). \tag{7}$$

In low Mach number flows, the challenge faced by standard hyperbolic numerical methods is that the system becomes stiff. The stiffness is caused by the stringent Courant-Friedrichs-Levy (CFL) restriction [3, 5, 6], i.e. $\Delta t \leq \Delta x / \max_i |\lambda_i| = \mathcal{O}(\varepsilon \Delta x)$ with the spatial and temporal grid sizes Δx and Δt. The restriction results in an increasingly large computational time for $\varepsilon \to 0$. Moreover, the strong stability requirement for $\varepsilon \to 0$ results in the excessive numerical viscosity of the standard hyperbolic solvers that is proportional to $\max_i |\lambda_i| = \mathcal{O}(\varepsilon^{-1})$. This makes the standard hyperbolic solvers suffer from severe loss of accuracy due to the creation of spurious waves. Therefore, the stability and accuracy of the standard hyperbolic numerical methods highly depend on ε [5].

In the literature, some all-speed schemes [3, 4, 7, 8, 9] have been derived for the compressible-incompressible limit problems based on the idea of the asymptotic-preserving (AP) methodology introduced by Jin [10, 11] for relaxation systems. The AP all-speed schemes are uniformly consistent with the low-Mach number limit and are uniformly stable. Although a robust AP scheme should allow both explicit and implicit time-marching techniques, the explicit strategies suffer from the CFL stability conditions and thus affect the efficiency of the method for small Mach numbers. The implicit strategies avoid the CFL restriction, but they need

to solve highly nonlinear equations and add an excessive numerical dissipation to the slow wave, degrading the accuracy of the method [3]. To overcome the drawbacks, the semi-implicit or implicit-explicit (IMEX) time discretization strategies are widely applied based on the acoustic/advection splitting of the Euler equations into the stiff/non-stiff parts (or fast and slow fluxes) [4, 5, 7, 9, 12, 13, 14, 15, 16]. These strategies treat with the stiff part implicitly and the non-stiff part explicitly to solve the isentropic Euler equations effectively and efficiently. The IMEX time discretization combined with the shock-capturing schemes, e.g., the first-order local Lax-Friedrichs (or Rusanov) scheme [5], the second-order finite volume method [3, 17], the arbitrary high order accurate discontinuous Galerkin method [18] and the fifth-order finite difference weighted essentially non-oscillatory (WENO) scheme [4] has been shown its good performances in compressible and incompressible regimes.

Recently a class of weighted compact nonlinear schemes (WCNS's) as high order accurate shock-capturing schemes have been widely adopted to investigate compressible flows with shock waves and discontinuities [19, 20, 21, 22, 23, 24, 25]. The WCNS's first proposed by Deng and Zhang [19] and developed in [20, 21, 22, 26] integrate WENO interpolation into the cell-centered compact schemes. They are variants of the WENO schemes and have the good performance in terms of accuracy, robustness and efficiency for compressible flows. Compared to the WENO schemes, the WCNS's feature a better spectral resolution at the same order of accuracy and are more flexible in the choice of flux splitting methods and flux derivatives can be computed by different explicit or implicit compact finite difference methods [21]. In this work, in view of the good performance of the IMEX time discretization method and the WCNS's, we design a high order IMEX WCNS for the all-Mach isentropic Euler system based on the acoustic/advection splitting strategy [4]. The stiff linear part governing fast acoustic and the non-stiff nonlinear part modeling slow nonlinear advection effects are solved by the high order implicit and explicit time discretization methods, respectively. In the zero Mach number limit, the high order IMEX WCNS has the AP property and is asymptotically stable under a convective CFL condition. One- and two-dimensional numerical examples are given to demonstrate good performance of the designed method in both compressible and incompressible regimes.

WCNS method

In this section, a fifth-order WCNS is considered for the spatial discretization. The WCNS procedure consists of three components, i.e., midpoint-to-node differencing, flux evaluation at the midpoint and node-to-midpoint weighted averaging interpolation of fluxes. Here, we briefly describe the framework of WCNS discretization for the first derivative, f_x, in the one-dimensional scalar case $u_t + f(u)_x = 0$. For simplicity, we take a uniform grid defined by $x_i = i\Delta x = ih, i = 0, ..., N$, where h is the uniform grid spacing and N is the number of cells.

An explicit central-type scheme [26] is applied to approximate f_x, i.e.,

$$f'_i = \frac{64}{45h}(\hat{f}_{i+1/2} - \hat{f}_{i-1/2}) - \frac{2}{9h}(f_{i+1} - f_{i-1}) + \frac{1}{180h}(f_{i+2} - f_{i-2}). \tag{8}$$

By the Taylor series expansion of (8), we obtain

$$f'_i = (f_x)_i - \frac{1}{5040}h^6(\frac{\partial^7 f}{\partial x^7})_i + O(h^8) + O(h^r), \tag{9}$$

where the truncation term $O(h^r)$ comes from the numerical approximations of the cell-edge fluxes $f_{i\pm1/2}$, denoted by $\hat{f}_{i\pm1/2}$. The accuracy of the scheme (8) is $min(6, r)$. Here, the numerical fluxes $\hat{f}_{i\pm1/2}$ approximate $f_{i\pm1/2}$ to the fifth order and thus a fifth-order WCNS is designed for the spatial discretization.

Various flux splitting methods [21] can be used in WCNS to introduce correct upwinding. For simplicity, we use the Lax-Friedrichs flux splitting, i.e., the flux is split into positive and negative parts:

$$f = f^+ + f^-, \quad f^\pm = \frac{1}{2}(f \pm \alpha u), \tag{10}$$

where $\alpha = \max_u |f'_u|$ is the maximum characteristic wave speed. The numerical fluxes $\hat{f}_{i\pm1/2}$ at the cell centers in (8) are calculated as

$$\hat{f}_{i\pm1/2} = \hat{f}^+_{i\pm1/2} \pm \hat{f}^-_{i\pm1/2}. \tag{11}$$

A fifth-order WENO interpolation technique is considered to obtain the positive numerical flux $\hat{f}^+_{i+1/2}$. The interpolation process of the negative numerical flux $\hat{f}^-_{i+1/2}$ is symmetric with respect to $x_{i+1/2}$ and will not be shown here. For simplicity, the "+" sign in the superscript is removed.

The numerical flux $\hat{f}_{i+1/2}$ on a cell center can be interpolated locally from the values on a five-point upwind-biased stencil $S = \{x_{i\pm2}, x_{i\pm1}, x_i\}$. The stencil S can be divided into three sub-stencils $S_k = \{x_{i+k-2}, x_{i+k-1}, x_{i+k}\}$, $k = 0, 1, 2$. On each sub-stencil a third-order linear interpolation of f at cell center $x_{i+1/2}$ can be derived, i.e.,

$$\hat{f}^0_{i+1/2} = \frac{1}{8}(3f_{i-2} - 10f_{i-1} + 15f_i), \tag{12}$$

$$\hat{f}^1_{i+1/2} = \frac{1}{8}(-f_{i-1} + 6f_i + 3f_{i+1}), \tag{13}$$

$$\hat{f}^2_{i+1/2} = \frac{1}{8}(3f_i + 6f_{i+1} - f_{i+2}), \tag{14}$$

where $\hat{f}^k_{i+1/2}, k = 0, 1, 2$, are the approximated values at cell center $x_{i+1/2}$ on $S_k, k = 0, 1, 2$, respectively. On the stencil S a fifth-order upwind-biased linear interpolation of f at cell center $x_{i+1/2}$ can be derived, i.e.,

$$\hat{f}^{upwind}_{i+1/2} = \frac{1}{128}(3f_{i-2} - 20f_{i-1} + 90f_i + 60f_{i+1} - 5f_{i+2}), \tag{15}$$

which can also be constructed linearly from the three third-order interpolations $\hat{f}^k_{i+1/2}$:

$$\hat{f}^{upwind}_{i+1/2} = \sum_{k=0}^{2} d_k \hat{f}^k_{i+1/2}, \tag{16}$$

with the linear weights

$$d_0 = \frac{1}{16}, \quad d_1 = \frac{10}{16}, \quad d_2 = \frac{5}{16}. \tag{17}$$

The central-type scheme (8) with the upwind-biased linear interpolation (15) or (16) will generate oscillations around shock waves and discontinuities. To capture shock waves and discontinuities, the numerical flux $\hat{f}_{i+1/2}$ should be computed by using the nonlinear combination of upwind-biased interpolations, i.e.,

$$\hat{f}_{i+1/2} = \sum_{k=0}^{2} \omega_k \hat{f}^k_{i+1/2}, \tag{18}$$

where $\omega_k, k = 0, 1, 2$, are the upwind-biased nonlinear weights that are associated with the relative smoothness of f on each sub-stencil. In smooth areas the nonlinear weights ω_k should be close to the linear weights d_k to achieve the design order and be close to zero near discontinuities to suppress spurious numerical oscillations near discontinuities.

There are several types of nonlinear weights ω_k in the literature, e.g., the WENO-JS [27], WENO-M [28] and WENO-Z [29, 30, 31] weights. The WENO-Z weights place a larger weight to the less smooth sub-stencil. They are less dissipative than the WENO-JS weights and more efficient than the WENO-M weights. Here, the WENO-Z weights ω_k proposed by Borges et al. [29] are chosen and defined as

$$\omega_k = \frac{\alpha_k}{\sum_{k=0}^{2} \alpha_k}, \quad \alpha_k = d_k \left(1 + \frac{\tau}{\beta_k + \delta}\right), \tag{19}$$

where the second-order smoothness indicators $\beta_k, k = 0, 1, 2$, derived by Hu [32] are adopted to measure the smoothness of f on the sub-stencils S_k and are defined as

$$\beta_k = \frac{1}{4}(a_k)^2 + \frac{13}{12}(b_k)^2 - |a_k b_k|, \tag{20}$$

with

$$a_0 = f_{i-2} - 4f_{i-1} + 3f_i, \quad a_1 = f_{i-1} - f_{i+1}, \quad a_2 = 3f_i - 4f_{i+1} + f_{i+2},$$
$$b_0 = f_{i-2} - 2f_{i-1} + f_i, \quad b_1 = f_{i-1} - 2f_i + f_{i+1}, \quad b_2 = f_i - 2f_{i+1} + f_{i+2}.$$

In (19), the global higher order smoothness indicator $\tau = |\beta_0 - \beta_2|$ and the parameter δ is a small constant to avoid denominators becoming zero.

Remark 1. The value of δ in (19) will influence the convergence, accuracy and stability of the schemes. Here, a parameter-free algorithm proposed by Zheng et al. [33] is used to calculate the value of δ as follows.

$$\delta = \frac{\beta_{ave}\beta_{min}}{\beta_{std}}, \tag{21}$$

where $\beta_{ave} = \frac{1}{3}\sum_{k=0}^{2} \beta_k$, $\beta_{min} = min\{\beta_0, \beta_1, \beta_2\}$, $\beta_{std} = \sqrt{\frac{1}{3}\sum_{k=0}^{2}(\beta_{ave} - \beta_k)^2}$. To avoid denominators becoming zero in (19) and (21), $\beta_k + \delta$ in (19) and β_{std} in

(21) are replaced with $max(\beta_k + \delta, err)$ and $max(\beta_{std}, err)$, respectively. Here, err is the square root of the smallest positive number allowed for a machine.

IMEX method

In this section, we briefly describe the framework of IMEX time discretization designed for the numerical integration of the stiff ordinary differential equation (ODE) as follows.

$$y_t = \bar{f}(y) + \bar{g}(y), \tag{22}$$

where $\bar{f}$ and $\bar{g}$ are the non-stiff and stiff parts of the ODE, respectively. The IMEX time discretization treats the non-stiff part explicitly and the stiff part implicitly in order to overcome the stringent time-step restriction for stability. There are many IMEX methods designed for various problems in the literature [34, 35, 36, 37, 38]. Among them, the IMEX Runge-Kutta (IMEX-RK) schemes as combinations of explicit RK methods and diagonally implicit A- or L-stable RK (DIRK) methods and with various orders of accuracy and numbers of stages offer a precise and robust approach to define high order AP schemes. The computational cost per time step is proportional to the number of stages in the IMEX-RK schemes and the accuracy is proportional to the time-step size and the order of accuracy.

In this paper, the L-stable IMEX-ARS$p(s, \sigma, p)$ scheme proposed by Ascher et al. [34] is used for the time discretization. This scheme with s stages of the implicit scheme for the stiff term and $\sigma(= s+1)$ stages of the explicit scheme for the non-stiff term has p^{th}-order temporal accuracy. The IMEX-ARS$p(s, \sigma, p)$ for Eq.(22) from t^n to t^{n+1} is described as

$$y^{(k)} = y^n + \Delta t \sum_{j=1}^{k-1} \tilde{a}_{kj} \bar{f}(y^{(j)}) + \Delta t \sum_{j=1}^{k-1} a_{kj} \bar{g}(y^{(j)}) + \Delta t a_{kk} \bar{g}(y^{(k)}), k = 1, ..., s, \tag{23}$$

$$y^{n+1} = y^n + \Delta t \sum_{k=1}^{s} \tilde{b}_k \bar{f}(y^{(k)}) + \Delta t \sum_{k=1}^{s} b_k \bar{g}(y^{(k)}). \tag{24}$$

The IMEX-ARS$p(s, \sigma, p)$ is characterized by the $s \times s$ matrices $\mathbf{A} = (a_{ij}), \tilde{\mathbf{A}} = (\tilde{a}_{ij})$, the vectors $\mathbf{b}, \tilde{\mathbf{b}} \in \mathbb{R}^s$, and the vectors $\mathbf{c}, \tilde{\mathbf{c}} \in \mathbb{R}^s$ [34]. Here, the matrices $\mathbf{A}, \tilde{\mathbf{A}}$ for the implicit and explicit schemes are described respectively as

$$\mathbf{A} = \begin{pmatrix} 0 & 0 \\ 0 & A_{22} \end{pmatrix}, \tilde{\mathbf{A}} = \begin{pmatrix} 0 & 0 \\ \tilde{A}_{21} & \tilde{A}_{22} \end{pmatrix}, \tag{25}$$

with the submatrices $(\tilde{A}_{21})_{(s-1)\times 1}, (\tilde{A}_{21})_{(s-1)\times(s-1)}$ and the invertible submatrix $(A_{22})_{(s-1)\times(s-1)}$.

Definition 1. The IMEX-ARSp scheme is of type ARS, i.e., the matrix $\mathbf{A}$ for the implicit scheme is described as in (25).

Definition 2. The IMEX-ARSp scheme is globally stiffly accurate (see [3, 4]), i.e., the matrices $\mathbf{A}, \tilde{\mathbf{A}}$ and the vectors $\mathbf{b}^T, \tilde{\mathbf{b}}^T$ satisfy

$$\mathbf{e}_s^T \mathbf{A} = \mathbf{b}^T, \quad \mathbf{e}_s^T \tilde{\mathbf{A}} = \tilde{\mathbf{b}}^T, \quad c_s = \tilde{c}_s = 1, \tag{26}$$

where $\mathbf{e}_s = (0, ..., 0, 1)^T$.

IMEX-ARSp WCNS

In this section, we design the IMEX-ARSp WCNS scheme for the isentropic Euler system. Here, the fifth-order WCNS described in the previous section is used for the spatial discretization and the p^{th}-order IMEX-ARSp method is used for the time discretization. We first split the Euler system into two parts based on the acoustic/advection splitting strategy [4] and obtain

$$\mathbf{U}_t = \mathbf{F} + \mathbf{G}, \tag{27}$$

where $\mathbf{U} = (\rho, \mathbf{q})$, $\mathbf{F} = -(0, \nabla \cdot \frac{\mathbf{q}\otimes\mathbf{q}}{\rho})$ is the non-stiff nonlinear term and $\mathbf{G} = -(\nabla \cdot \mathbf{q}, \frac{1}{\varepsilon^2}\nabla p)$ is the stiff linear term.

The p^{th}-order IMEX-ARSp scheme that consists of (23) and (24) is applied to each component of (27). The intermediate stages are described as

$$\rho^{(k)} = \rho^n - \Delta t \sum_{j=1}^{k-1} a_{kj} \nabla \cdot \mathbf{q}^{(j)} - \Delta t a_{kk} \nabla \cdot \mathbf{q}^{(k)}, \tag{28}$$

$$\mathbf{q}^{(k)} = \mathbf{q}^n - \Delta t \sum_{j=1}^{k-1} \tilde{a}_{kj} \left(\nabla \cdot \frac{\mathbf{q} \otimes \mathbf{q}}{\rho} \right)^{(j)} - \Delta t \sum_{j=1}^{k-1} a_{kj} \frac{1}{\varepsilon^2} \nabla p^{(j)} - \Delta t a_{kk} \frac{1}{\varepsilon^2} \nabla p^{(k)}, \tag{29}$$

where $k = 1, 2, ..., s$, and the numerical solutions at time t^{n+1} are described as

$$\rho^{n+1} = \rho^n - \Delta t \sum_{k=1}^{s} b_k \nabla \cdot \mathbf{q}^{(k)}, \tag{30}$$

$$\mathbf{q}^{n+1} = \mathbf{q}^n - \Delta t \sum_{k=1}^{s} \tilde{b}_k \left(\nabla \cdot \frac{\mathbf{q} \otimes \mathbf{q}}{\rho} \right)^{(k)} - \Delta t \sum_{k=1}^{s} b_k \frac{1}{\varepsilon^2} \nabla p^{(k)}. \tag{31}$$

The intermediate stages (28) and (29) consist of two implicit steps and can be simplified by eliminating $\mathbf{q}^{(k)}$ between (28) and (29) [4], and obtain a nonlinear elliptic equation for $\rho^{(k)}$:

$$-\frac{(\Delta t a_{kk})^2}{\varepsilon^2} \triangle p(\rho^{(k)}) + \rho^{(k)} = \hat{\rho}^{(k)} - \Delta t a_{kk} \nabla \cdot \hat{\mathbf{q}}^{(k)}, \tag{32}$$

where

$$\hat{\rho}^{(k)} = \rho^n - \Delta t \sum_{j=1}^{k-1} a_{kj} \nabla \cdot \mathbf{q}^{(j)}, \tag{33}$$

$$\hat{\mathbf{q}}^{(k)} = \mathbf{q}^n - \Delta t \sum_{j=1}^{k-1} \tilde{a}_{kj} \left(\nabla \cdot \frac{\mathbf{q} \otimes \mathbf{q}}{\rho} \right)^{(j)} - \Delta t \sum_{j=1}^{k-1} a_{kj} \frac{1}{\varepsilon^2} \nabla p^{(j)}. \tag{34}$$

Based on (29) and (34), $\mathbf{q}^{(k)}$ can be calculated as

$$\mathbf{q}^{(k)} = \hat{\mathbf{q}}^{(k)} - \Delta t a_{kk} \frac{1}{\varepsilon^2} \nabla p^{(k)}. \tag{35}$$

Remark 2. To update the solutions from t^n to t^{n+1} by the p^{th}-order IMEX-ARSp WCNS, we first solve the elliptic equation (32) to obtain $\rho^{(k)}$ and then calculate explicitly $\mathbf{q}^{(k)}$ using (35). Here, (32) is a nonlinear equation for $\rho^{(k)}$, which is solved by inexact Newton-generalized minimum residual (Newton-GMRES) algorithms. Refer to [39, 40] for the detailed description of the algorithms. Finally, the updates ρ^{n+1} and $\mathbf{q}^{n+1}$ are calculated explicitly using (30) and (31) with the intermediate values $\rho^{(k)}$ and $\mathbf{q}^{(k)}$.

Remark 3. The spatial discretization of both convective terms in (32)-(34) and the gradient terms in (33) and (34) are solved by the fifth-order WCNS in the component-by-component and dimension-by-dimension forms. Here, in the interpolation process of the cell-edge pressures, the Lax-Friedrichs flux with zero numerical viscosity is considered, i.e., $p = \frac{1}{2}p + \frac{1}{2}p$, otherwise the numerical diffusion will become large when $\varepsilon \to 0$ [4].

Remark 4. The CFL stability condition for the explicit time discretization is

$$\Delta t \leq CFL \cdot h/(\underset{\mathbf{u}\cdot\mathbf{n},\rho}{max}|\mathbf{u}\cdot\mathbf{n}| + \sqrt{p'(\rho)}/\varepsilon) = O(\varepsilon) \xrightarrow{\varepsilon\to 0} 0, \tag{36}$$

which leads to unaffordable computational costs in the low Mach number regime. The time-step size Δt for the IMEX-ARSp time discretization is

$$\Delta t \leq CFL \cdot h/\alpha, \tag{37}$$

where $\alpha = \underset{\mathbf{u}\cdot\mathbf{n},\rho}{max}|\mathbf{u}\cdot\mathbf{n}| + min(1, 1/\varepsilon)\sqrt{p'(\rho)}$. For $\varepsilon \geq 1$, the condition (37) is equivalent to the classical CFL condition (36), but for $\varepsilon \to 0$ it is independent of the Mach number ε and thus is less restrictive. Therefore, the IMEX-ARSp time discretization is more efficient than the explicit time discretization for low-Mach number flows.

Remark 5. For one-dimensional case, the term $\triangle p = p_{xx}$ in (32) is approximated by a fourth-order central-type difference scheme:

$$p_i'' = \frac{-p_{i-2} + 16p_{i-1} - 30p_i + 16p_{i+1} - p_{i+2}}{12h^2}. \tag{38}$$

For two-dimensional case, this central-type difference scheme in a dimension-by-dimension form is applied to $\triangle p = p_{xx} + p_{yy}$.

AP property

Definition 3. A scheme for the low Mach number limit of the Euler equations is asymptotic preserving, if it serves as a consistent and stable discretisation, independent the Mach number ε.

Proposition 1. Consider the system (1) subject to well-prepared initial data (i.e., $\rho_0^0 = const, \nabla \cdot \mathbf{u}_0^0(\mathbf{x}) = 0$) and periodic, wall or homogeneous Neumann boundary conditions. The IMEX-ARSp WCNS ((28)-(31)) that is of type ARS and globally stiffly accurate (see Definitions 1 and 2) is applied to solve (1) from $t = t^0$ to t^1 with the time-step size $\Delta t = t^1 - t^0$ given by the stability condition (37) that is independent of ε, and we then have

$$\rho^1(\mathbf{x}, t^1) \xrightarrow{\varepsilon\to 0} \rho_0^0, \quad \nabla \cdot \mathbf{u}^1(\mathbf{x}, t^1) \xrightarrow{\varepsilon\to 0} 0, \tag{39}$$

and

$$\mathbf{u}^1(\mathbf{x},t^1) \xrightarrow{\varepsilon\to 0} \mathbf{u}_e(\mathbf{x},t^1)+O(\Delta t^{p+1}). \tag{40}$$

Here, $\mathbf{u}_e$ is the exact solution of the imcompressible Euler equations (5) with initial data $\mathbf{u}_e(\mathbf{x},0)=\mathbf{u}_0^0(\mathbf{x})$.

Let $\mathbf{f}=\nabla\cdot\frac{\mathbf{q}\otimes\mathbf{q}}{\rho}$, $\vec{r}=(r^{(1)},...,r^{(s)})^T$ for $r=\rho$ or p, and $\vec{\mathbf{v}}=(\mathbf{v}^{(1)},...,\mathbf{v}^{(s)})^T$ for $\mathbf{v}=\mathbf{f}$ or $\mathbf{q}$ generated at the IMEX-ARSp intermediate stages $t_k=t^0+c_k\Delta t$. Following [4], we give the proof process of Proposition 1.

Proof. Based on (28)-(31), we obtain from $t=t^0$ to t^1

$$\begin{aligned}\vec{\rho} &= \rho^0\mathbf{e}-\Delta t\mathbf{A}\nabla\cdot\vec{\mathbf{q}}, &(41)\\ \vec{\mathbf{q}} &= \mathbf{q}^0\mathbf{e}-\Delta t\tilde{\mathbf{A}}\nabla\cdot\vec{\mathbf{f}}-\frac{\Delta t}{\varepsilon^2}\mathbf{A}\nabla\vec{p}, &(42)\end{aligned}$$

and

$$\begin{aligned}\rho^1 &= \rho^0-\Delta t\mathbf{b}^T\nabla\cdot\vec{\mathbf{q}}, &(43)\\ \mathbf{q}^1 &= \mathbf{q}^0-\Delta t\tilde{\mathbf{b}}^T\nabla\cdot\vec{\mathbf{f}}-\frac{\Delta t}{\varepsilon^2}\mathbf{b}^T\nabla\vec{p}, &(44)\end{aligned}$$

where $\mathbf{e}=(1,...,1)^T\in\mathbb{R}^s$.

Taking the divergence of both sides of (42) and substituting $\nabla\cdot\vec{\mathbf{q}}$ into (41) yields a pressure Poisson equation

$$\frac{\Delta t^2}{\varepsilon^2}\mathbf{A}^2\triangle\vec{p}=(\vec{\rho}-\rho^0\mathbf{e})+\Delta t\mathbf{A}\nabla\cdot\mathbf{q}^0\mathbf{e}-\Delta t^2\mathbf{A}\tilde{\mathbf{A}}\nabla\cdot(\nabla\cdot\vec{\mathbf{f}}). \tag{45}$$

In order to study the asymptotic behavior of the solutions, we plug the ε-asymptotic expansions $f(\mathbf{x})=f_0(\mathbf{x})+\varepsilon^2 f_2(\mathbf{x})+O(\varepsilon^3)$ for variables $\vec{\rho},\rho^1,\vec{p},p^1$ and $g(\mathbf{x})=g_0(\mathbf{x})+O(\varepsilon^2)$ for variables $\vec{\mathbf{q}},\mathbf{q}^1$ into (41)-(45). At the leading order $O(\varepsilon^{-2})$ terms in (42), we obtain $\nabla\vec{p}_0=\nabla\vec{p}(\vec{\rho}_0)=0$. Therefore, $\vec{p}_0$ and $\vec{\rho}_0$ are independent of $\mathbf{x}$. Collecting the order $O(1)$ terms in ε generates

$$\begin{aligned}\vec{\rho}_0-\rho_0^0\mathbf{e} &= -\Delta t\mathbf{A}\nabla\cdot\vec{\mathbf{q}}_0, &(46)\\ \vec{\mathbf{q}}_0-\mathbf{q}_0^0\mathbf{e} &= -\Delta t\tilde{\mathbf{A}}\nabla\cdot\vec{\mathbf{f}}_0-\Delta t\mathbf{A}\nabla\vec{p}_2, &(47)\\ \rho_0^1-\rho_0^0 &= -\Delta t\mathbf{b}^T\nabla\cdot\vec{\mathbf{q}}_0, &(48)\\ \mathbf{q}_0^1-\mathbf{q}_0^0 &= -\Delta t\tilde{\mathbf{b}}^T\nabla\cdot\vec{\mathbf{f}}_0-\Delta t\mathbf{b}^T\nabla\vec{p}_2, &(49)\\ \Delta t^2\mathbf{A}^2\triangle\vec{p}_2 &= \vec{\rho}_0-\rho_0^0\mathbf{e}+\Delta t\mathbf{A}\nabla\cdot\mathbf{q}_0^0\mathbf{e}-\Delta t^2\mathbf{A}\tilde{\mathbf{A}}\nabla\cdot(\nabla\cdot\vec{\mathbf{f}}_0), &(50)\end{aligned}$$

where $\mathbf{q}_0^0=\rho_0^0\mathbf{u}_0^0$ and $\vec{\mathbf{f}}_0=\vec{\mathbf{q}}_0\otimes\vec{\mathbf{q}}_0/\vec{\rho}_0$.

Integrating (46) over the whole computational domain and applying periodic, wall or homogeneous Neumann boundary conditions yields $\vec{\rho}_0=\rho_0^0\mathbf{e}$, i.e., $\vec{\rho}_0$ is independent of t. Since $\vec{\rho}_0=\rho_0^0\mathbf{e}$ and $\nabla\cdot\mathbf{q}_0^0=\rho_0^0\nabla\cdot\mathbf{u}_0^0=0$, (50) becomes

$$\mathbf{A}^2\triangle\vec{p}_2=-\mathbf{A}\tilde{\mathbf{A}}\nabla\cdot(\nabla\cdot\vec{\mathbf{f}}_0). \tag{51}$$

Based on Definition 1, (51) can be simplified as

$$\triangle \vec{p}_2' = -A_{22}^{-1}(\tilde{A}_{21}\nabla\cdot(\nabla\cdot\vec{\mathbf{f}}_0^{(1)}) + \tilde{A}_{22}\nabla\cdot(\nabla\cdot\vec{\mathbf{f}}_0')), \tag{52}$$

where $\vec{p}' = (p^{(2)}, ..., p^{(s)})^T$ and $\vec{\mathbf{f}}_0' = (\mathbf{f}^{(2)}, ..., \mathbf{f}^{(s)})^T$.

Taking the divergence of both sides of (47) and applying Definition 1 and (52) yields

$$\vec{\mathbf{q}}_0 = 0, \quad \vec{\mathbf{u}}_0 = 0. \tag{53}$$

Based on (48) and (53), we have $\rho_0^1 = \rho_0^0$, i.e., $\rho^1(\mathbf{x}, t^1) \xrightarrow{\varepsilon\to 0} \rho_0^0$. Taking the divergence of both sides of (49) and applying Definition 2 generates

$$\nabla\cdot\mathbf{q}_0^1 = -\Delta t\mathbf{e}_s^T(\tilde{\mathbf{A}}\nabla\cdot(\nabla\cdot\vec{\mathbf{f}}_0) + \mathbf{A}\triangle\vec{p}_2). \tag{54}$$

By applying Definition 1 and (52), (54) is simplified as $\nabla\cdot\mathbf{q}_0^1 = \rho^1\nabla\cdot\mathbf{u}_0^1 = 0$. Since $\rho_0^1 = \rho_0^0$, we have $\nabla\cdot\mathbf{u}_0^1 = 0$, i.e., $\nabla\cdot\mathbf{u}^1(\mathbf{x}, t^1) \xrightarrow{\varepsilon\to 0} 0$.

Both sides of (47) and (49) are divided by the constant density ρ_0^0 and we obtain the asymptotic limit of scheme for the incompressible Euler system (5):

$$\vec{\mathbf{u}}_0 = \mathbf{u}_0^0\mathbf{e} - \Delta t\tilde{\mathbf{A}}\frac{1}{\rho_0^0}\nabla\cdot\vec{\mathbf{f}}_0 - \Delta t\mathbf{A}\frac{1}{\rho_0^0}\nabla\vec{p}_2, \tag{55}$$

$$\mathbf{u}_0^1 = \mathbf{u}_0^0 - \Delta t\tilde{\mathbf{b}}^T\frac{1}{\rho_0^0}\nabla\cdot\vec{\mathbf{f}}_0 - \Delta t\mathbf{b}^T\frac{1}{\rho_0^0}\nabla\vec{p}_2, \tag{56}$$

where $\vec{p}_2$ is given by (51). If the IMEX-ARSp WCNS that has p^{th}-order temporal accuracy is adopted to solve the system (5) subject to initial data $\mathbf{u}_e(\mathbf{x}, 0) = \mathbf{u}_0^0$, the asymptotic accuracy can be attained, i.e., (40) is proved.

Remark 6. A similar procedure can be adopted when going from t^n to t^{n+1} to prove that the limiting IMEX-ARSp WCNS is a consistent discretization of the limiting equation for fixed h and Δt. The IMEX-ARSp WCNS is also asymptotically stable with the time-step restriction (37) independent of the Mach number ε.

Numerical examples

The third-order IMEX-ARS3 WCNS is applied to solve the following numerical examples. In addition, a third-order explicit total variation diminishing Runge-Kutta time-stepping method [27] coupled with the fifth-order WCNS (TVD-RK3 WCNS) is used to solve some examples for comparisons. The order of temporal accuracy is numerically calculated as

$$p = \log_2(E_{\Delta t_1}/E_{\Delta t_2}), \tag{57}$$

where $E_{\Delta t_1}$ obtained with $\Delta t_1 = O(h)$ and $E_{\Delta t_2}$ obtained with $\Delta t_2 = \Delta t_1/2$ are the global errors in the L^1 norm, respectively. The space-step size h deceases with the time-step size Δt.

Example 1. Convergence test for one-dimensional case [3]

This example is adopted to test the temporal order of accuracy of the IMEX-ARS3 WCNS for one-dimensional case. The computational domain is $[-2.5, 2.5]$ with periodic boundary conditions. The initial data for one-dimensional isentropic Euler equations (1) is given by

$$u(x,0) = sin\left(\frac{2\pi x}{L}\right), \quad \rho(x,0) = \left(1 + \frac{(\gamma-1)u(x,0)}{c}\right)^2, \quad p = \rho^\gamma, \tag{58}$$

where $\gamma = 2, c = 2\sqrt{\gamma}/\varepsilon, L = 5$ and the final time is fixed to $T_f = 0.3$. The solution computed on a fine mesh with $N = 2560$ cells is used as a reference ("exact") solution since the exact solution of this problem is unknown. Table 1 reports the numerical L^1-norm errors and orders of accuracy in time for the density based on different values of the Mach number. It is observed that the IMEX-ARS3 WCNS shows a third-order temporal convergence, as expected, for different values of the Mach number, from compressible to incompressible regimes.

Example 2. One-dimensional Riemann problem [4, 5, 6]

This example that consists in several interacting Riemann problems is used to validate the asymptotic stability of the IMEX-ARS3 WCNS. The computational domain is $[0, 1]$ with periodic boundary conditions. The initial data is described as

$$\begin{cases} \rho(x,0) &= 1, & q(x,t) = 1 - 0.5\varepsilon^2, & x \in [0, 0.2] \cup [0.8, 1], \\ \rho(x,0) &= 1 + \varepsilon^2, & q(x,t) = 1, & x \in [0.2, 0.3], \\ \rho(x,0) &= 1, & q(x,t) = 1 + 0.5\varepsilon^2, & x \in [0.3, 0.7], \\ \rho(x,0) &= 1 - \varepsilon^2, & q(x,t) = 1, & x \in [0.7, 0.8], \end{cases} \tag{59}$$

and the pressure is $p(\rho) = \rho^2$. The final time is fixed to $T_f = 0.05$. The values of the Mach number are chosen as $\varepsilon = \sqrt{0.99}, 0.3, 0.01$ corresponding to the compressible, intermediate and incompressible regimes, respectively. The numerical solution calculated by the IMEX-ARS3 WCNS with $N = 200$ cells is compared to a reference solution computed by the third-order TVD-RK3 WCNS with $N = 2000$ cells. Figure 1 illustrates the solutions for the density and momentum. From this figure, we observe the two methods can capture shocks and contact discontinuities that are stronger when ε is bigger. Numerical nonphysical oscillations are observed with the TVD-RK3 WCNS when $\varepsilon = \sqrt{0.99}$. Compared to the TVD-RK3 WCNS, the IMEX-ARS3 WCNS with the AP property captures the limit incompressible solution faster when ε is small. When ε approaches 0, the TVD-RK3 WCNS can not capture the correct solution, due to the excessive numerical viscosity.

Example 3. Convergence test for two-dimensional case [17]

This example that is used to test the temporal order of accuracy of the IMEX-ARS3 WCNS for two-dimensional case is given in a computational domain $[0, 1] \times [0, 1]$ with periodic boundary conditions. The pressure is $p(\rho) = \frac{1}{2}\rho^2$. The final time is $T_f = 0.02$. The initial data is given by the following exact solution

$$\begin{cases} \rho(\mathbf{x},t) &= 1 + \varepsilon^2 \frac{1.5^2}{16\pi^2}\delta(r)(k(r) - k(\pi)), \\ u(\mathbf{x},t) &= 0.6 + 1.5(1 + \cos(r))\delta(r)(0.5 - y), \\ v(\mathbf{x},t) &= 1.5(1 + \cos(r))\delta(r)(x - 0.6t - 0.5), \end{cases} \tag{60}$$

where $r = 4\pi\sqrt{(x-0.6t-0.5)^2+(y-0.5)^2}$, $k(r) = 2\cos(r) + 2r\sin(r) + 0.125\cos(2r) + 0.25r\sin(2r) + 0.75r^2$ and

$$\delta(r) = \begin{cases} 1, & r < \pi, \\ 0, & otherwise. \end{cases} \tag{61}$$

Table 2 shows the numerical L^1-norm errors and orders of accuracy in time for the momentum ρu based on different values of the Mach number, from compressible to incompressible regimes, which validates the IMEX-ARS3 WCNS for two-dimensional case can attain the designed temporal accuracy.

Example 4. Two-dimensional Riemann problem [4, 7]

This example is used to test the performance of the IMEX-ARS3 WCNS at a high Mach number for two-dimensional case. The computational domain $[0,1]\times[0,1]$ with zero Neumann boundary conditions. The pressure is $p(\rho) = \rho^{1.4}$. This initial data includes four shock waves and is described as

$$(\rho, u, v) = \begin{cases} (0.1308, 1.206, 1.206), & x < 0.5, y < 0.5, \\ (0.5323, 0.000, 1.206), & x \geq 0.5, y < 0.5, \\ (0.5323, 1.206, 0.000), & x < 0.5, y \geq 0.5, \\ (1.5000, 0.000, 0.000), & otherwise. \end{cases} \tag{62}$$

The values of the Mach number are chosen as $\varepsilon = 1$ and 2 to test the robust shock-capturing capability of the IMEX-ARS3 WCNS in the compressible regime. Figure 2 plots the surfaces of the density profile obtained with the IMEX-ARS3 WCNS and the third-order TVD-RK3 WCNS on a mesh 50×50 at $T_f = 0.1$. From this figure, we see that two methods reproduce almost the same numerical results and the IMEX-ARS3 WCNS has a slightly higher resolution.

Example 5. Cylindrical explosion problem [6, 9]

The computational domain is $[-1,1] \times [-1,1]$ with periodic boundary conditions and the pressure is given by $p(\rho) = \rho^2$. The initial density of the fluid is given by

$$\begin{cases} \rho(\mathbf{x}, 0) = 1 + \varepsilon^2, & if\ r < 0.5, \\ \rho(\mathbf{x}, 0) = 1, & otherwise, \end{cases} \tag{63}$$

where $r = \sqrt{x^2+y^2}$ is the distance to the center $(0,0)$ of the domain. The initial velocity of the fluid is given by

$$\begin{cases} u(\mathbf{x}, 0) = -\frac{x}{r}\frac{\beta}{\rho(\mathbf{x},0)}, \\ v(\mathbf{x}, 0) = -\frac{y}{r}\frac{\beta}{\rho(\mathbf{x},0)}, \end{cases} \tag{64}$$

where $\beta = max(0, 1-r)e^{-16r^2}$ and $(u, v) = (0, 0)$, if $r \leq 10^{-15}$. The computational domain is divided into 50×50 cells. Figure 3 plots the surface of the density profile and the velocity field for $\varepsilon = 1$ obtained with the IMEX-ARS3 WCNS at time $t = 0.1, 0.25$ and 0.5, respectively. Figure 4 show the density profile and the discrete divergence of the velocity $\nabla \cdot \mathbf{u}$ at time $t = 0.05$ for a small value of $\varepsilon = 0.001$. It

is observed that when $\varepsilon = 0.001$, the density converges to the constant value 1 and the divergence $\nabla \cdot \mathbf{u}$ is close to 0.

Example 6. Shear flow problem [3, 4, 16]

This example is used to verify numerically the AP property of the IMEX-ARS3 WCNS in the low Mach number limit. The computational domain is $[0, 2\pi] \times [0, 2\pi]$ with periodic boundary conditions and the pressure is set to $p(\rho) = \rho^{1.4}$. Initially, a constant density and an incompressible velocity field are given by $\rho(\mathbf{x}, 0) = \pi/15$ and

$$u(\mathbf{x}, 0) = \begin{cases} \tanh((y - 0.5\pi)/\rho), & y \leq \pi, \\ \tanh((1.5\pi - y)/\rho), & otherwise, \end{cases} \qquad v(\mathbf{x}, 0) = 0.05 \sin(x). \tag{65}$$

The Mach number is $\varepsilon = 10^{-4}$ and the final time is $T_f = 10$. Figure 5 demonstrates the discrete vorticity $\omega = v_x - u_y$ on a mesh 50×50 at different times. From this figure, we see the vorticity quickly develops into roll-ups with smaller and smaller scales with the time evolution. Figure 6 shows the time history of the L_1-norm error of the discrete divergence of the velocity $\nabla \cdot \mathbf{u}$. It is observed that the L_1-norm error increases with time, which is in agreement with the phenomenon in [4] and is caused by the appearance of the smaller and smaller scale structures in the shear flow.

Example 7. Kelvin-Helmholtz instability problem [4]

This problem is solved in the domain $[0, 2\pi] \times [0, 4\pi]$ with periodic boundary conditions. The pressure is $p(\rho) = \rho^2$ and the initial data reads

$$\rho(\mathbf{x}, 0) = 1, \quad u(\mathbf{x}, 0) = \cos(y), \quad v(\mathbf{x}, 0) = 0.03 \sin(0.5x). \tag{66}$$

The Mach number is $\varepsilon = 10^{-3}$ and the final time is $T_f = 40$. The discrete vorticity $\omega = v_x - u_y$ on a mesh 50×50 at different times is depicted in Figure 7, which shows the emergence and subsequent evolution of small scale flow features. The time history of the L_1-norm error of the discrete divergence of the velocity $\nabla \cdot \mathbf{u}$ is shown in Figure 8, from which we also observe that the L_1-norm error increases with time and the maximum error is smaller than that obtained with a finer mesh in [4].

Conclusions

In this work, we have designed a high order IMEX WCNS for the compressible-incompressible limit problems that are described as scaled isentropic Euler equations. Based on an acoustic/advection splitting strategy, the semi-implicit method is composed of the third-order IMEX-ARS3 scheme for the time integration and the fifth-order WCNS for the spatial discretization. This method has been proven to be asymptotic preserving, i.e., it converges to a consistent scheme in the zero Mach number limit, and asymptotically stable under a convective CFL condition. This method has also been verified numerically that it can achieve a third-order temporal accuracy for different values of the Mach number, from compressible to incompressible regimes. Numerical results show that the IMEX WCNS with the AP property can capture shocks and contact discontinuities with high resolution in

the compressible regime, while it can capture incompressible features in the imcompressible regime. The future work is to extend this designed IMEX WCNS with the AP property for compressible Navier-Stokes flows at any Mach number.

Abbreviations

WCNS: Weighted compact nonlinear scheme

IMEX: Implicit-explicit

CFL: Courant-Friedrichs-Levy

AP: Asymptotic-preserving

WENO: Weighted essentially non-oscillatory

ODE: Ordinary differential equation

RK: Runge-Kutta

DIRK: Diagonally implicit Runge-Kutta

Newton-GMRES: Newton-generalized minimum residual

TVD-RK3: Third-order total variation diminishing Runge-Kutta

Declarations

Availability of data and materials
All data generated or analysed during this study are included in this published article.

Competing interests
The authors declare that they have no competing interests.

Funding
The present study is supported by the National Numerical Wind Tunnel Project (No. NNW2018-ZT4A08), the National Natural Science Foundation of China (Nos. 11872323 and 11971025) and the Natural Science Foundation of Fujian Province (No. 2019J06002)

Author's contributions
These authors contributed equally to this work.

Acknowledgements
Not applicable.

Author details
[1]Department of Mathematics, Southwest University of Science and Technology, 621010 Mianyang, China. [2]School of Mathematical Sciences, Fujian Provincial Key Laboratory of Mathematical Modeling and High-Performance Scientific Computing, Xiamen University, 361005 Xiamen, China. [3]Computational Aerodynamics Institute, China Aerodynamics Research and Development Center, 621000 Mianyang, China.

References

1. Klainerman, S., Majda, A.: Singular limits of quasilinear hyperbolic systems with large parameters and the incompressible limit of compressible fluids. Commun Pure Appl Math **34**, 481–524 (1981)
2. Klainerman, S., Majda, A.: Compressible and incompressible fluids. Commun Pure Appl Math **35**, 629–653 (1982)
3. Boscarino, S., Russo, G., Scandurra, L.: All Mach number second order semi-implicit scheme for the Euler equations of gas dynamics. J Sci Comput **77**, 850–884 (2018)
4. Boscarino, S., Qiu, J.M., Russo, G., Xiong, T.: A high order semi-implicit imex weno scheme for the all-Mach isentropic Euler system. J Comput Phys **392**, 594–618 (2019)
5. Degond, P., Tang, M.: All speed scheme for the low Mach number limit of the isentropic Euler equations. Commun Comput I Phys **10**, 1–31 (2011)
6. Dimarco, G., Vignal, M.H., Loubère, R.: Study of a new asymptotic preserving scheme for the Euler system in the low Mach number limit. SIAM J Sci Comput **39**, 2099–2128 (2017)
7. Haack, J., Jin, S., Liu, J.G.: An all-speed asymptotic-preserving method for the isentropic Euler and Navier-Stokes equations. Commun Comput Phys **12**, 955–980 (2012)
8. Cordier, F., Degond, P., Kumbaro, A.: An asymptotic-preserving all speed scheme for the Euler and Navier-Stokes equations. J Comput Phys **231**, 5685–5704 (2012)
9. Goudon, T., Llobell, J., Minjeaud, S.: An asymptotic preserving scheme on staggered grids for the barotropic Euler system in low Mach regimes. Numer Meth Part D E **0**, 1–31 (2020)

10. Jin, S.: Efficient asymptotic-preserving (AP) schemes for some multiscale kinetic equations. SIAM J Sci Comput **21**, 441–454 (1999)
11. Jin, S.: Asymptotic preserving (AP) schemes for multiscale kinetic and hyperbolic equations: A review. Riv Mat Univ Parma **3**, 177–216 (2012)
12. Klein, R.: Semi-implicit extension of a Godunov-type scheme based on low Mach number asymptotics I. One-dimensional flow. J Comput Phys **121**, 213–237 (1995)
13. Noelle, S., Bispen, G., Arun, K.R., Lukáčová-Medvid'ová, M., Munz, C.-D.: A weakly asymptotic preserving low Mach number scheme for the euler equations of gas dynamics. SIAM J Sci Comput **36**, 989–1024 (2014)
14. Bispen, G., Lukacova-Medvidova, M., Yelash, L.: Asymptotic preserving IMEX finite volume schemes for low Mach number Euler equations with gravitation. J Comput Phys **335**, 222–248 (2017)
15. Zakerzadeh, H., Noelle, S.: A note on the stability of implicit-explicit flux-splittings for stiff systems of hyperbolic conservation laws. Commun Math Sci **16**, 1–15 (2018)
16. Dimarco, G., Loubere, R., D., V.M., Vignal, M.H.: Second order Implicit-Explicit Total Variation Diminishing schemes for the Euler system in the low Mach regime. J Comput Phys **372**, 178–201 (2018)
17. Arun, K.R., Samantaray, S.: Asymptotic preserving and low Mach number accurate IMEX finite volume schemes for the Euler Equations. arXiv e-prints (2019)
18. Tavelli, M., Dumbser, M.: A pressure-based semi-implicit space-time discontinuous galerkin method on staggered unstructured meshes for the solution of the compressible Navier-Stokes equations at all Mach numbers. J Comput Phys **341**, 341–376 (2017)
19. Deng, X.G., Zhang, H.X.: Developing high-order weighted compact nonlinear schemes. J Comput Phys **165**, 22–44 (2000)
20. Zhang, S., Jiang, S., Shu, C.-W.: Development of nonlinear weighted compact schemes with increasingly higher order accuracy. J Comput Phys **227**, 7294–7321 (2008)
21. Nonomura, T., Fujii, K.: Robust explicit formulation of weighted compact nonlinear scheme. Comput Fluids **85**, 8–18 (2013)
22. Liu, X., Zhang, S., Zhang, H., Shu, C.-W.: A new class of central compact schemes with spectral-like resolution II: hybrid weighted nonlinear schemes. J Comput Phys **284**, 133–154 (2015)
23. Deng, X.G., Mao, M.L., Jiang, Y., Liu, H.Y.: New high-order hybrid cell-edge and cell-node weighted compact nonlinear schemes. AIAA paper 2011-3857
24. Yan, Z.-G., Liu, H.Y., Ma, Y.K., Mao, M.L., Deng, X.G.: Further improvement of weighted compact nonlinear scheme using compact nonlinear interpolation. Comput Fluids **156**, 135–145 (2017)
25. Wong, M.L., Lele, S.K.: High-order localized dissipation weighted compact nonlinear scheme for shock- and interface-capturing in compressible flows. J Comput Phys **339**, 179–209 (2017)
26. Deng, X., Jiang, Y., Mao, M., Liu, H., Li, S., Tu, G.: A family of hybrid cell-edge and cell-node dissipative compact schemes satisfying geometric conservation law. Comput Fluids **116**, 29–45 (2015)
27. Jiang, G.-S., Shu, C.-W.: Efficient implementation of Weighted ENO schemes. J Comput Phys **126**, 202–228 (1996)
28. Henrick, A.K., Aslam, T.D., Powers, J.M.: Mapped weighted essentially nonoscillatory schemes: achieving optimal order near critical points. J Comput Phys **207**, 542–567 (2005)
29. Borges, R., Carmona, M., Costa, B., Don, W.S.: An improved weighted essentially non-oscillatory scheme for hyperbolic conservation laws. J Comput Phys **227**, 3191–3211 (2008)
30. Liu, S., Shen, Y., Zeng, F., Yu, M.: A new weighting method for improving the WENO-Z scheme. Int J Numer Meth Fluids **87**, 271–291 (2018)
31. Xin, L., Songping, W.: An improved fifth-order WENO-Z+ scheme. Chinese J Theor App Mech **51**, 1927–1939 (2019)
32. Hu, F.: The weighted ENO scheme based on the modified smoothness indicator. Comput Fluids **150**, 1–7 (2017)
33. Zheng, S., Deng, X., Wang, D., Xie, C.: A parameter-free ϵ-adaptive algorithm for improving weighted compact nonlinear schemes. Int J Numer Meth Fluids **90**, 247–266 (2019)
34. Ascher, U.M., Ruuth, S.J., Spiteri, R.J.: Implicit-explicit Runge-Kutta methods for time-dependent partial differential equations. Appl Numer Math **25**, 151–167 (1997)
35. Kennedy, C.A., Carpenter, M.H.: Additive Runge-Kutta schemes for convection-diffusion-reaction equations. Appl Numer Math **44**, 139–181 (2003)
36. Pareschi, L., Russo, G.: Implicit-Explicit Runge-Kutta schemes and applications to hyperbolic systems with relaxation. J Sci Comput **25**, 129–155 (2005)
37. Boscarino, S.: (2007)
38. S.Boscarino, Pareschi, L., Russo, G.: Implicit-explicit Runge-Kutta schemes for hyperbolic systems and kinetic equations in the diffusion limit. SIAM J Sci Comput **35**, 22–51 (2013)
39. Kelley, C.: Iterative Methods for Linear and Nonlinear Equations. Society for Industrial and Applied Mathematics, New Haven (1995)
40. Botti, L.: A choice of forcing terms in inexact Newton iterations with application to pseudo-transient continuation for incompressible fluid flow computations. Appl Math Comput **266**, 713–737 (2015)

Figures

Tables

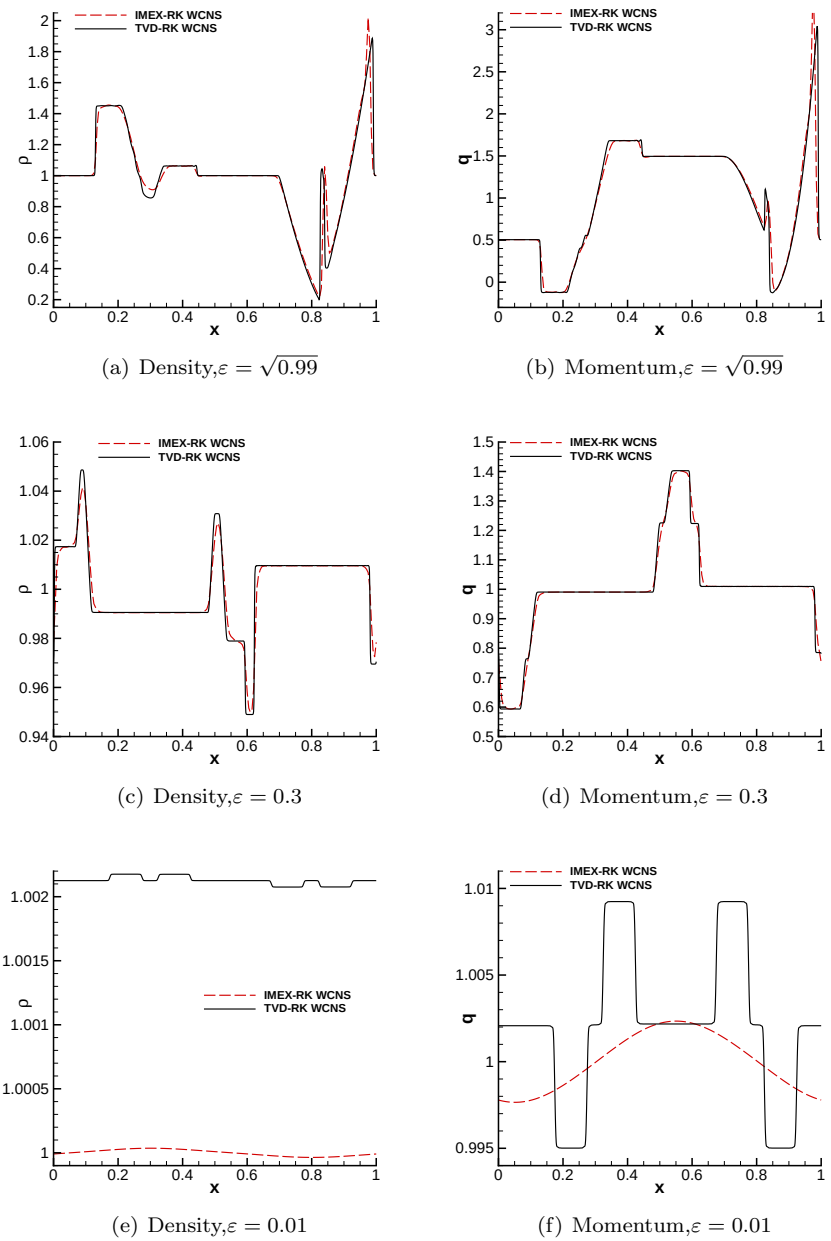

(a) Density,$\varepsilon = \sqrt{0.99}$ (b) Momentum,$\varepsilon = \sqrt{0.99}$

(c) Density,$\varepsilon = 0.3$ (d) Momentum,$\varepsilon = 0.3$

(e) Density,$\varepsilon = 0.01$ (f) Momentum,$\varepsilon = 0.01$

Figure 1 Example 2. Density (left) and momentum (right) calculated by the IMEX-ARS3 WCNS with $N = 200$ cells and the TVD-RK3 WCNS with $N = 2000$ cells at $t = 0.05$. The values of the Mach number are $\varepsilon = \sqrt{0.99}$ (top), 0.3 (middle) and 0.05 (bottom).

Table 1 L^1 errors and numerical orders of temporal accuracy for Example 1 obtained with the IMEX WCNS at $t = 0.3$.

N	$\varepsilon = 0.01$		$\varepsilon = 0.1$		$\varepsilon = 1$	
	L^1 error	Order	L^1 error	Order	L^1 error	Order
20	$5.72E-04$		$1.08E-03$		$5.14E-03$	
40	$1.32E-04$	2.12	$1.93E-04$	2.49	$5.58E-04$	3.20
80	$2.29E-05$	2.53	$2.87E-05$	2.75	$3.09E-05$	4.17
160	$3.29E-06$	2.80	$3.86E-06$	2.90	$8.75E-07$	5.14
320	$4.31E-07$	2.93	$5.04E-07$	2.94	$6.14E-08$	3.83

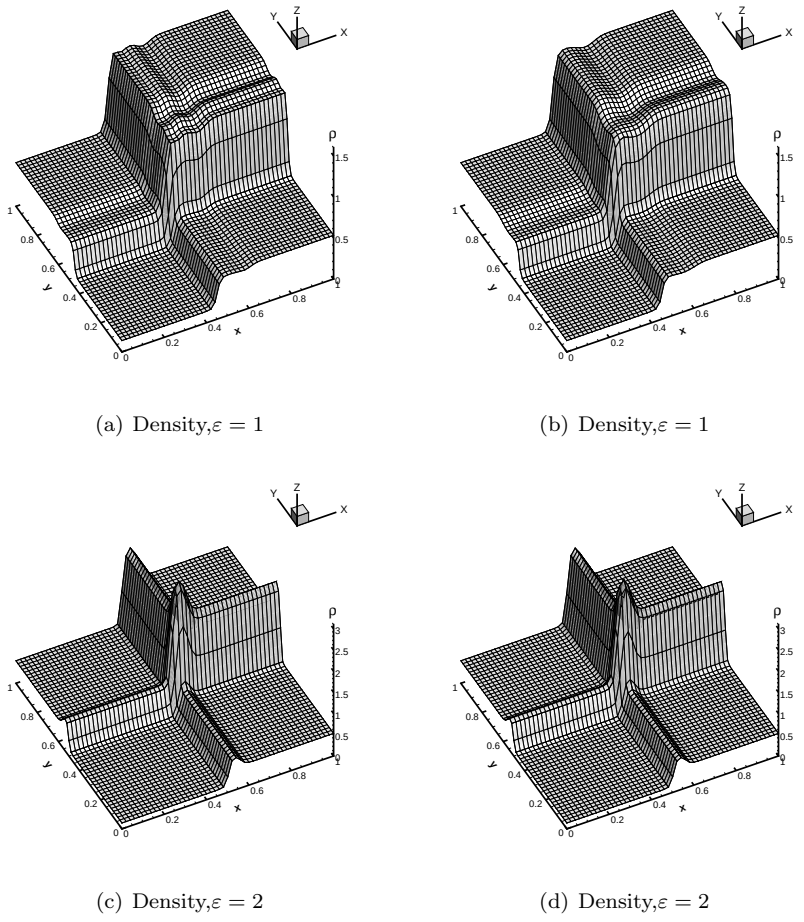

(a) Density,$\varepsilon = 1$ (b) Density,$\varepsilon = 1$

(c) Density,$\varepsilon = 2$ (d) Density,$\varepsilon = 2$

Figure 2 Example 4. Density obtained with the IMEX-ARS3 WCNS (left) and the TVD-RK3 WCNS (right) on a mesh 50×50 at $t = 0.1$. The values of the Mach number are $\varepsilon = 1$ (top) and 2 (bottom).

Table 2 L^1 errors and numerical orders of temporal accuracy for Example 3 obtained with the IMEX WCNS at $t = 0.02$.

$M \times N$	$\varepsilon = 0.01$		$\varepsilon = 0.1$		$\varepsilon = 1$	
	L^1 error	Order	L^1 error	Order	L^1 error	Order
20×20	$8.78E-04$		$4.21E-04$		$3.18E-04$	
40×40	$2.53E-04$	1.80	$9.10E-05$	2.21	$7.35E-05$	2.12
80×80	$6.32E-05$	2.00	$1.90E-05$	2.26	$1.60E-05$	2.20
160×160	$6.69E-06$	3.24	$3.02E-06$	2.65	$2.69E-06$	2.58
320×320	$4.36E-07$	3.94	$3.40E-07$	3.15	$3.44E-07$	2.96

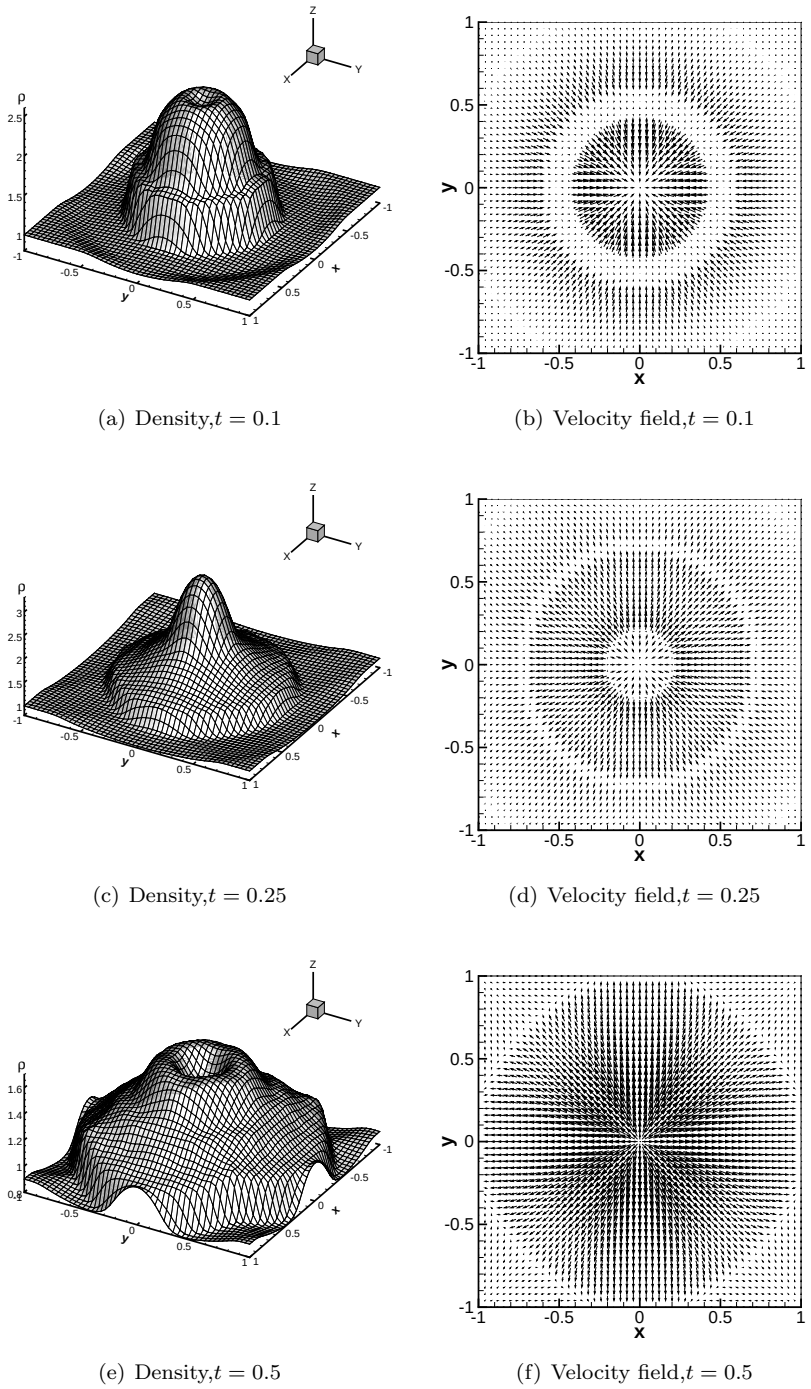

(a) Density,$t = 0.1$ (b) Velocity field,$t = 0.1$

(c) Density,$t = 0.25$ (d) Velocity field,$t = 0.25$

(e) Density,$t = 0.5$ (f) Velocity field,$t = 0.5$

Figure 3 Example 5. Density (left) and velocity field (right) calculated by the IMEX-ARS3 WCNS on a mesh 50×50 at different times.

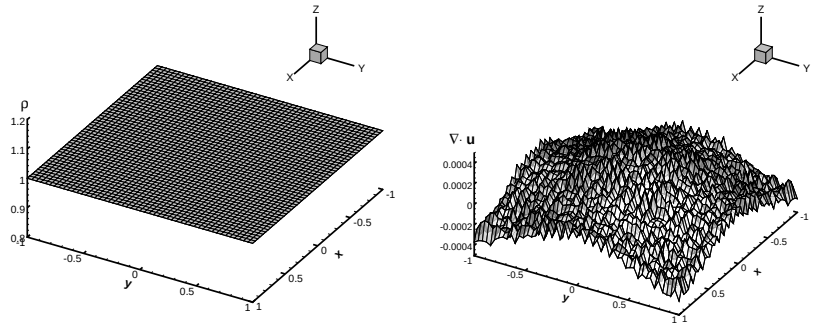

(a) Density,$\varepsilon = 0.001$ (b) Divergence,$\varepsilon = 0.001$

Figure 4 Example 5. Density (left) and divergence (right) calculated by the IMEX-ARS3 WCNS on a mesh 50×50 at $t = 0.05$.

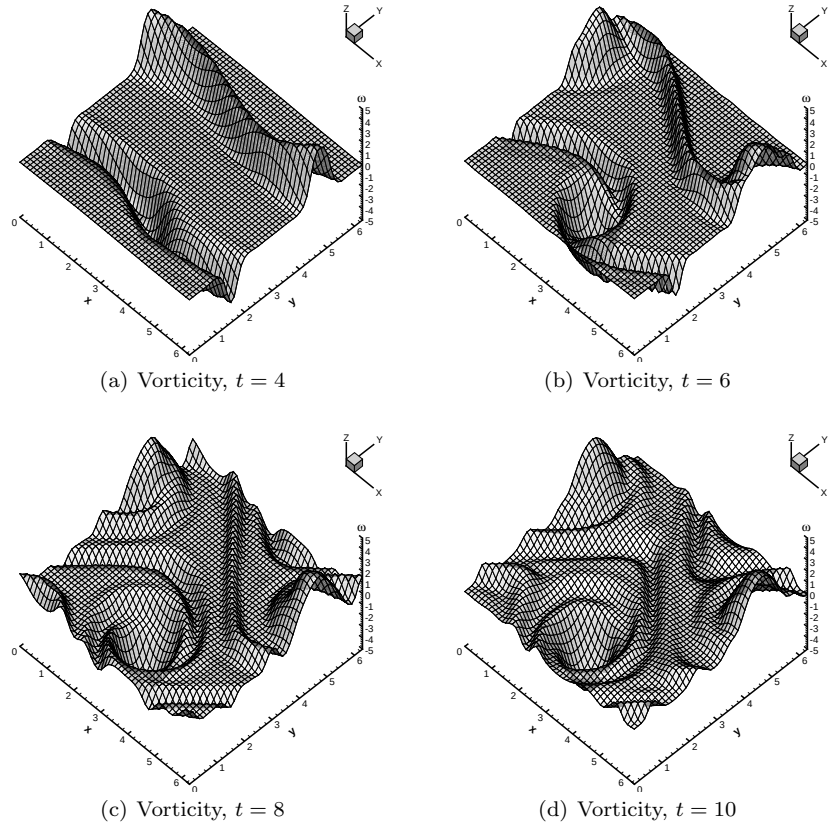

(a) Vorticity, $t = 4$ (b) Vorticity, $t = 6$

(c) Vorticity, $t = 8$ (d) Vorticity, $t = 10$

Figure 5 Example 6. Vorticity $\omega = v_x - u_y$ obtained with the IMEX-ARS3 WCNS on a mesh 50×50 at different times.

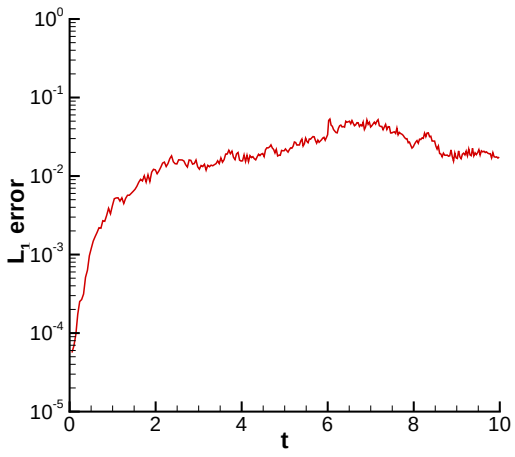

Figure 6 Example 6. Time history of L_1 error of the divergence of the velocity $\nabla \cdot \mathbf{u}$.

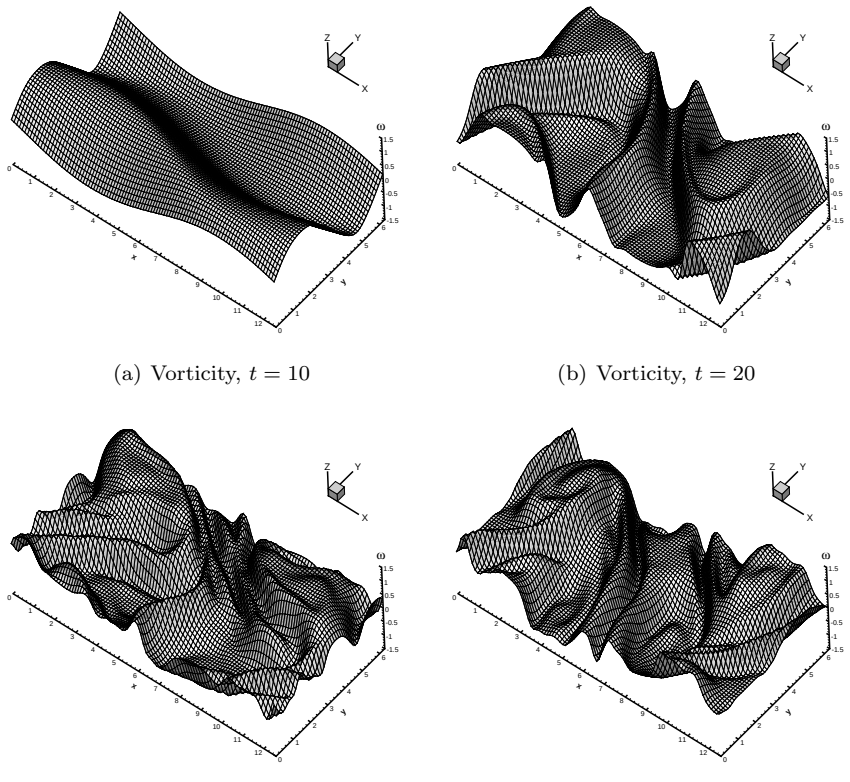

(a) Vorticity, $t = 10$ (b) Vorticity, $t = 20$

(c) Vorticity, $t = 30$ (d) Vorticity, $t = 40$

Figure 7 Example 7. Vorticity $\omega = v_x - u_y$ obtained with the IMEX-ARS3 WCNS on a mesh 50×50 at different times.

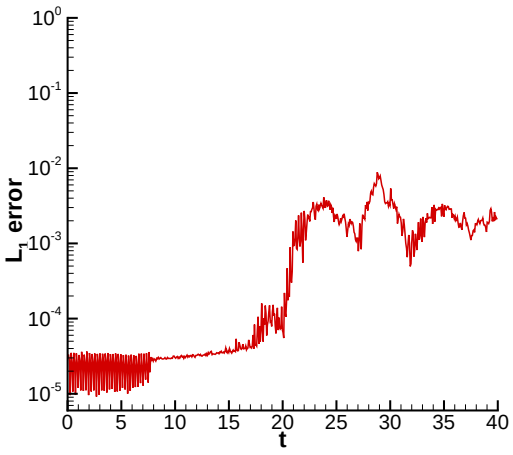

Figure 8 Example 7. Time history of L_1 error of the divergence of the velocity $\nabla \cdot \mathbf{u}$.